Journal of Colloid and Interface Science 560 (2020) 618–625

Contents lists available at ScienceDirect

Journal of Colloid and Interface Science

journal homepage: www.elsevier.com/locate/jcis

Regular Article

Alignment of worm-like micelles at intermediate and high shear rates

Brisa Arenas-Gómez [a,b,1], Cristina Garza [d], Yun Liu [b,c], Rolando Castillo [d,*]

[a] *División de Ciencias e Ingenierías, Campus León, Universidad de Guanajuato, Loma del Bosque 103, Lomas del Campestre, 37150 León, Guanajuato, Mexico*
[b] *Center for Neutron Research, National Institute of Standards and Technology, Gaithersburg, MD 20899, USA*
[c] *Department of Chemical and Biomolecular Engineering, University of Delaware, Newark, DE 19716, USA*
[d] *Instituto de Física, Universidad Nacional Autónoma de México, P.O. Box 20-364, 01000 México City, Mexico*

GRAPHICAL ABSTRACT

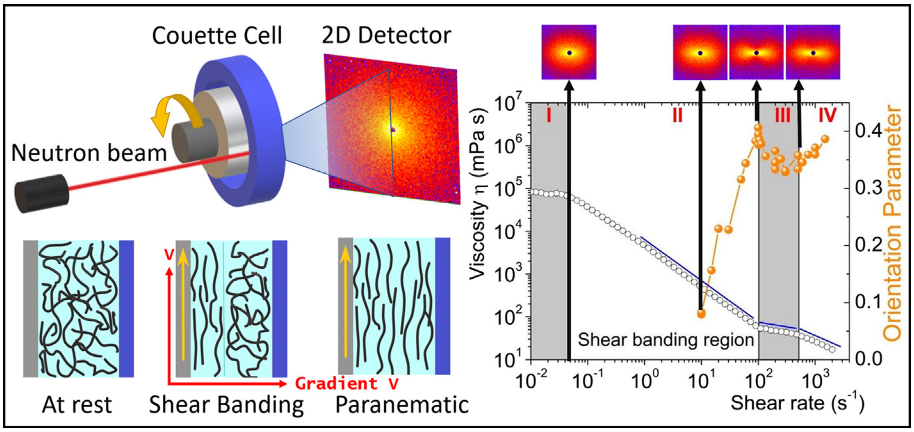

ARTICLE INFO

Article history:
Received 27 June 2019
Revised 12 October 2019
Accepted 14 October 2019
Available online 19 October 2019

Keywords:
Small-angle neutron scattering (SANS)
Rheo-SANS
Shear banding
Wormlike micelle orientation order

ABSTRACT

Hypothesis: Rheology combined with Small-Angle Neutron Scattering (Rheo-SANS) can determine the local structural order in Worm-Like Micelle (WLM) solutions when the shear rate increases beyond the ending of the gradient shear banding. There, micelles are supposedly aligned, but viscosity reveals a transition regime as the shear rate increases.
Experiments: The mixture of 3-[dimethyl(tetradecyl)azaniumyl]propane-1-sulfonate (TDPS), sodium dodecylsulfate (SDS) (*R = [SDS]/[TDPS]* = 0.55), and a water solution of NaCl (0.2 mol/L), was studied with mechanical rheology and Small-Angle Neutron Scattering (SANS) in the quiescent fluid and under flow.
Findings: The system self-assembles in WLMs and presents gradient shear banding. SANS patterns of the bands formed during the shear banding were obtained in a Couette geometry along the 1–2 plane, as well as the orientation parameter along the gap. At very high shear rates, in the paranematic phase, we found an apparent transition on the flow curves with its corresponding change in the orientation parameter. The origin of this transition is unclear, but we present possible explanations of why we observe it.

1. Introduction

When steadily sheared, several complex fluids may separate into bands of different local viscosities and internal structuring

---

* Corresponding author.
E-mail address: rolandoc@fisica.unam.mx (R. Castillo).
[1] Present address: Departamento de Fisica, Universidad Autonoma Metropolitana-Iztapalapa, Cd. Mexico 09340, Mexico.

https://doi.org/10.1016/j.jcis.2019.10.052

[1,2]. This behavior is known as shear banding. It involves inhomogeneous flows, where macroscopic bands bearing different local shear rates or shear stresses coexist in the fluid. Shear banding can be observed under flow, along the gradient or vorticity directions. Rehage and Hoffmann [3] showed the first experimental evidence of a stress plateau in nonlinear rheological measurements on WLM solutions. It was recognized, almost immediately, that the plateau is associated with a nonuniform flow. Since then, these self-assembled surfactant systems forming long, cylindrical, and semiflexible aggregates have arisen as a model system to study gradient shear banding. The rheological signature of gradient shear banding is the presence of an almost horizontal stress plateau in the flow curve $\sigma(\dot{\gamma})$. Here, the micellar solution undergoes a shear-induced transition from a viscoelastic state of entangled micelles to a state with highly aligned micelles above some shear rate $\dot{\gamma}_1$ (paranematic phase). Such a transition is strongly shear-thinning because the viscosity of the aligned state is much smaller than the zero-shear viscosity of the system. Under simple shear in a Couette cell and above a critical $\dot{\gamma}_1$, the system spatially separates into two coexisting bands of high and low viscosities η_1 and η_2 corresponding to the entangled and aligned states, respectively. As the shear rate increases above $\dot{\gamma}_1$, the shear-induced alignment progressively grows along the velocity gradient direction at almost constant shear stress. This situation evolves until the system at some shear rate, $\dot{\gamma}_2$, is fully aligned. Several rheo-optical methods have been used to observe and determine the structure of the bands experimentally, namely flow birefringence in Couette geometry, [4,5] sheet of light in an optical rheometry, [6,7] nuclear magnetic resonance, [8] flow in microfluidic channels, [9–11] and scattering measurements employing small angles in light, [12] X-ray, [13] or neutron scattering [14,15] depending on the characteristic length scale of the microstructure to be probed. Also, pointwise velocity measurements have been used to characterize the flow field in the bands, to determine whether the shear rate profile is indeed constituted of bands of different viscosities and if the lever rule is obeyed (simple scenario) [16], i.e., $\dot{\gamma} = (1-\alpha)\dot{\gamma}_1 + \alpha\dot{\gamma}_2$, α gives the proportion of the shear-induced state along the stress plateau. The most commonly used techniques are NMR velocimetry, [8] particle tracking velocimetry, [17] photon correlation spectroscopy, [18] ultrasonic velocimetry, [19] and neutron scattering [20].

From the theoretical point of view, the origin of the gradient shear bands is the existence of a multivalued non-monotonic constitutive curve relating shear stress and shear rate in a homogeneous flow [1]. Here, the stress increases linearly with increasing $\dot{\gamma}$, passing through a maximum and then through a minimum before increasing again. This nonlinearity arises from the coupling between flow and mesostructure, where flow reorganizes mesostructure, which feeds back on the flow. The two branches of the constitutive curve, one at low and another at high shear rates, are separated by an unstable mechanical regime where $\frac{d\sigma}{d\dot{\gamma}} < 0$. Mechanical stability requires a separation of the fluid into bands at $\dot{\gamma}_1 < \dot{\gamma} < \dot{\gamma}_2$, where shear stress is almost constant throughout the fluid and bands show different shear rates. A widespread model to describe the mentioned nonlinearities is the phenomenologically motivated Johnson-Segalman model [21]. When this model includes a slip parameter, it supports shear bands. If also it includes a diffusive term, the flow can be heterogeneous with an interfacial width; the model is named as the non-local diffusive Johnson-Segalman model [22]. For an imposed shear rate in the negatively sloping regime, the instability triggers the formation of shear bands. If one is confined to calculations in one dimension and along the flow-gradient direction, the model predicts a steady coexistence of two bands, one for each of the positively sloping branches of the constitutive curve, with uniform shear stress, and separated by a stationary flat interface. The non-equilibrium phases obey the lever rule. If there is a concentration coupling, the stress plateau acquires a non-zero slope. However, in higher spatial dimensions, it predicts that the interface between the bands is linearly unstable due to normal stress effects. Nonlinear effects provide some stabilizing effect, causing the instability to saturate in traveling or rippling wavelike undulations along with the interface [14].

Rheo-SANS methods have been used to determine flow-induced structures in a variety of soft materials for almost four decades. These methods are capable of probing microstructure in the three shear planes of a Couette geometry: the 1–3 (flow-vorticity or velocity-vorticity) plane, the 2–3 (gradient-vorticity or velocity gradient-vorticity) plane, and the 1–2 (flow-gradient or velocity-velocity gradient) plane; [14] see Supplemental Material (SM). Since WLMs tend to show strong alignment in the flow direction during shear flow, then spatially-resolved flow-SANS measurements in the 1–2 plane are especially useful in detecting shear banding, and spatially-dependent microstructure information that enables us to determine the location of the shear band interface. There are characteristic differences in the 2D SANS patterns in the shear banding region ($\dot{\gamma}_1 < \dot{\gamma} < \dot{\gamma}_2$), and non-shear banding regions ($\dot{\gamma} < \dot{\gamma}_1$and $\dot{\gamma} > \dot{\gamma}_2$). In the region with bands, a significant and often discontinuous change in alignment is observed moving the position of the neutron beam along the gap in a Couette geometry. The discontinuity in the alignment along the gap is evidence of the coexistence of a band with highly aligned structures with another with non-aligned structures corresponding to the low and high viscosity bands, respectively. While shear banding is common in WLM solutions, altering solution composition or temperature can result in morphological changes such as micelle branching that may affect rheology and shear banding. Rheo-SANS methods in linear and branched WLMs have shown that branching may alter or eliminate the shear banding behavior of micellar solutions [23,24].

Several systems present the described simple shear banding scenario. At the end of the shear banding, the Couette cell geometry is full of the aligned phase. The micelle solution presents an almost constant viscosity ($\dot{\gamma} \geq \dot{\gamma}_2$, region III of Fig. 1 for the case of 40 °C). However, in some systems at specific thermodynamic conditions, if the shear rate is further increased, we observe a clear shear-thinning (region IV, Fig. 1). This effect, as far as we know, has not been studied. Most rheological and Rheo-SANS studies conclude at the end of the shear banding without reaching higher shear rates [13,24]. In this report, we present features that occur after the onset of the gradient shear banding ($0.06\ \mathrm{s}^{-1} < \dot{\gamma} < 100\ \mathrm{s}^{-1}$), especially at the high shear rates ($100\ \mathrm{s}^{-1} > \dot{\gamma}$). Therefore, we will examine regions II, III, and IV of a WLM solution made of TDPS, SDS, and water with NaCl using Rheo-SANS. Rheology and micro-rheology of this system have been previously investigated by our group [6,7,25].

2. Experimental section

2.1. Materials

3-[dimethyl(tetradecyl)azaniumyl]propane-1-sulfonate (CAS No: 14933-09-6; common name: *N*-Tetradecyl-*N*,*N*-Dimethyl-3-ammonio-1-Propane Sulfonate (TDPS, >99%) and sodium chloride (>99%) were from Sigma–Aldrich (USA), sodium dodecylsulfate (SDS, >99%) from Merck (Germany), and Phosphotungstic acid from Baker (Mexico) in water solution at 3% w/w. All the reagents are used as received. SANS samples are prepared using deuterated water (D_2O, 99.9%) from Cambridge Isotope Labs (USA) to reduce incoherent background and enhance the nuclear contrast.

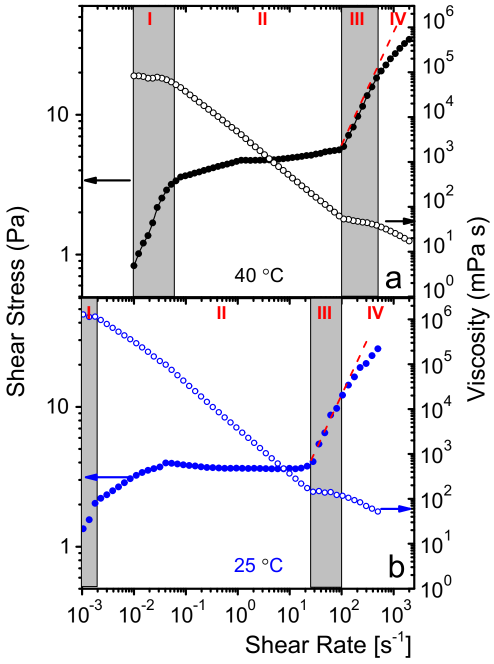

Fig. 1. (a) Shear stress (left, full circles) and viscosity (right, open circles) *vs.* shear rate for the system TDPS/SDS/D_2O at *40* °C, ($C_z = 46$ mmol/L, $[SDS]/[TDPS] = 0.55$, $C_{NaCl} = 0.2$ mol/L). I: No shear banding region, the system is formed by entangled and weakly oriented micelles <0.06 s^{-1}; II: Gradient shear banding region with two bands, 0.06 <$\dot{\gamma}$ <100 s^{-1}; III: above $\dot{\gamma} = 100$ s^{-1}, no shear banding, highly oriented micelles (paranematic phase). IV: Above$\dot{\gamma}$ ~500 s^{-1}, the system presents a shear-thinning of unclear origin. The red dashed line shows the slope change from region III to IV. (b) For comparison, we included data at 25 °C for this system, which presents a small shift to the left (viscosity blue open circles and shear stress blue full circles). I: Region without shear banding $\dot{\gamma} < 0.002$ s^{-1}. II: Gradient shear banding with two bands: $0.002 < \dot{\gamma} < 25$ s^{-1}. III: $\dot{\gamma} > 25$ s^{-1}, highly oriented micelles. IV: $\dot{\gamma} > 100$ s^{-1}, the system also presents shear thinning. Flow curves measured with a ME 21 Mooney-Eward Cony cylinder.

2.2. Sample preparation.

TDPS/SDS micelle solutions are made of a zwitterionic surfactant concentration of $C_z = 46$ mmol/L, where SDS is added to maintain a specific surfactant ratio ($R = [SDS]/[TDPS] = 0.55$). NaCl is also added to the micellar solution to get a salt concentration of 0.2 mol/L. Measurements are made at least two days after the solution preparation to allow them to reach equilibrium.

2.3. Rheology.

Rheological measurements are carried out in two different rheometers, both under strain-controlled conditions. An MCR 702 Anton Paar rheometer is used with a Couette geometry with a moving inner cylinder of $R_{in} = 5.00$ mm and outer cylinder of $R_{out} = 5.35$ mm; the temperature is held at 25 and 40 °C. Samples are allowed to rest before the measurements and loaded at 40 °C to prevent bubbles. Steady shear flow sweeps are performed logarithmically, increasing, and decreasing the shear rate from 0.01 to 1500 s^{-1}. Rheological measurements of the micellar solutions are replicated during SANS experiments, but now the solvent is deuterated water. For these experiments, an MCR 301 Anton-Paar rheometer is used. Measurements are repeated with different geometries at the same experimental conditions to ensure reproducibility, and to avoid slip-induced artifacts: cone-plate (CP 50-2), and concentric cylinders (CC 27, and a ME 21 Mooney-Eward Cony cylinder). To extend flow curves to high shear rates, the Mooney-Eward Cony cylinder geometry is used with a solvent trap with D_2O; Inner cylinder radius = 10.50 mm, cone angle = 3.18°, and gap = 0.6 mm.

2.4. Static small-angle neutron scattering (SANS)

Measurements in dilute samples were carried out on the NG7 SANS beamline at NIST Center for Neutron Research (NCNR) in Gaithersburg, MD. Three sample-detector distances were needed to have a broad scattering vector range: 1 m with eight beam guides, 4 m with four beam guides, and 15.3 m with lens (no guides). In all measurements, we used an incident neutron beam with a wavelength $\lambda = 6$ Å, and a wavelength spread of $\Delta\lambda/\lambda = 0.1$. The samples are measured at a constant temperature of *20* °C, in demountable Ti cells with a path length of 2 mm, and with windows made of quartz. Data coming from scattering are averaged over a period of time of 2000 s. After correcting the raw data for transmission, scattering of the solvent, and the empty cell measurements, the isotropic pattern is circularly averaged and converted to an absolute scale. For data reduction and analysis the Igor Pro SANS software is used according to standard methods [26].

2.5. Flow SANS

In the *1–2* (flow-gradient) plane, Rheo-SANS measurements are performed on NGB10m SANS instrument, also at the NCNR. Scattering experiments are carried out with neutrons of $\lambda = 5$ *Å* and $\Delta\lambda/\lambda = 0.1$, with a sample to detector distance of 2.5 m. The beam is directed on micellar solutions, under a specifically imposed shear rate deformation, in an aluminum Couette geometry with a gap width, *H*, of 1.35 mm. As shown in the schematics of Fig. 4a, this custom Couette cell consists of a rotating inner cylinder with $R_{in} = 25.11$ mm and a stationary outer cylindrical cup with $R_{out} = 26.5$ mm previously described [28,20]. The beam path is 5 mm. The rotor is housed in an aluminum frame containing the outer cylinder. The rotating inner cylinder is driven by a strain-controlled stepper motor with controlled shear rates up to 3500 s^{-1}. A frame with a small translating stepper motor moves a cadmium slit with an opening of 0.1 mm, along the Couette cell gap, which is covered with a quartz window. The slit is used to make the spatially resolved SANS measurements across the gap, and it is moved in steps of 0.1 mm from the inner wall to the outer wall of the cell. The motor position is calibrated to obtain a correct alignment and orientation of the cell with respect to the beamline [28]. A flow-through port within the cell is connected to a controlled ethylene glycol bath used to control the cell temperature. Shear-induced alignment is qualitatively seen in *2D* anisotropic scattering patterns. For spatially-resolved flow SANS, eight spaced normalized gap positions r/H were selected, from *0.29* to *0.8* for each applied shear rate of interest (including 0 s^{-1}). Transmission measurements at these gap positions are made with and without samples to normalize scattering data. When the shear rate slowly decreases in steps from 1500 to 10 s^{-1}, the detected SANS patterns are averaged over 2000 s to obtain proper statistics. Standard methods are used to reduce SANS data.

3. Results and discussion

3.1. Structure of the aggregates in the micellar solution

3.1.1. SANS results

For the first time, we measured the static SANS pattern of the TDPS/SDS system in a deuterated water solution at $C_z = 5$ mmol/L ($R = [SDS]/[TDPS] = 0.55$, $C_{NaCl} = 0.2$ mol/L), *i.e.*, in the dilute regime. Due to the isotropic nature of the scattering of the micellar solutions, the SANS intensity is circularly averaged and presented as a function of q in Fig. 2. The scattering patterns cover q values from 3×10^{-3} to 0.5 $Å^{-1}$, which correspond to length scales of $2\pi/q \sim 12–2100$ Å. For flexible cylindrical structures, the scattering window involves the analysis of three different regions: The low and intermediate q Guinier regions, and the Porod region, at high q [29,30]. In the instrument configuration of our experiment, the low-q Guinier region is not accessible. At the intermediate-q values, the scattering pattern displays a $\sim q^{-1}$ dependence, which is indicative of long cylindrical-shaped structures. At high q, the scattering comes from the local cross-section of tube-shaped aggregates. At intermediate q for cylindrical aggregates, the scattering function can be written as by $I(q)q = K\ \chi\ \exp(-q^2R^2_{g-cs}/2)$; χ is a constant linked to the size of the cylindrical aggregates, and $R_{g\text{-}cs}$ = the cross-sectional radius-of-gyration. $K = (b_m - V_m\rho_s)^2$ gives the contrast factor, ρ_s is the solvent scattering length density, V_m = volume per surfactant monomer in the micelle, and b_m is the sum of neutron scattering lengths. The cylinder radius is $R_{CS} = \sqrt{2}\ R_{g-cs}$, when the cross-section is circular with a uniform density distribution, [29,31] An intermediate Guinier fit for the TDPS/SDS system is presented in the inset of Fig. 2. The linearity of data indicates the extended cylindrical nature of the micelles. Fitting gives an average cross-section diameter of 4.7 ± 0.01 nm. The error only considers the statistical error during the fitting.

The scattering function exhibits an inflection point at $q \sim 0.005$ $Å^{-1}$, which is an indication of the micelle flexibility (Fig. 2). Therefore, a monodisperse flexible cylinder model is used to fit the data, where the scattering intensity is given by the form factor of a flexible cylinder with a circular cross-section, and a constant scattering length density. Intermicellar interactions and volume interactions within the walk of a single cylinder are not included in this model. A Schulz distribution is employed to include the polydispersity of the cross-section radius. This model was originally developed by Peterson and Schurtenberger to describe a system of semiflexible chains [27]. Later, Chen *et al.* suggested corrections for the excluded volume effects [32]. The total length L_C can be described as a chain of some number of locally stiff segments of length l_p. The persistence length is related to the Kuhn length, b, as $b = 2l_p$. Inter-cylinder interactions are not included in this model. In the model, the scattering function is expressed as $I(q, Lc, b) = A_C M_W \langle P(q, Lc, b)\rangle + background$, where A is a constant including the contrast and the specific micellar volume, and *background* is the residual scattering from the solvent. $\langle P(q, Lc, b)\rangle$ is the micellar form factor averaged over the molecular weight distribution that can be deconvoluted into two contributions $\langle P(q,Lc,b)\rangle = S_{WC}(q, L_C, b)\ P_{CS}(q, R_{CS})$. $S_{WC}(q, L_C, b)$ is due to a single semiflexible chain with excluded volume effects and $P_{CS}(q, R_{CS})$ to the local cylindrical cross-section structure:

$$P_{CS}(q, R_{CS}) = \left[\frac{2j_1(qR_{CS})}{qR_{CS}}\right]^2$$

$$\begin{aligned} S_{WC}(q, L_C, b) = {} & [1 - w(qR_g)]S_{Debye}(q, L_c, b) + w(q, R_G)[1.22(qR_g)^{(-1/\nu)} \\ & + 0.42(qR_g)^{(-2/\nu)} - 1.651(qR_g)^{(-3/\nu)}] \\ & + C\left(\frac{L_C}{b}\right)\left(\frac{b}{15L_C}\right)\left(4 + \frac{7}{u} - \left(11 - \frac{7}{u}\right)e^{(-u)}\right) \end{aligned}$$

Here, R_g is the radius-of-gyration of a chain with excluded volume effects, $w(qR_g)$ is an empirical crossover function, and S_{Debye} is the Debye function with $u = \langle R_g^2\rangle\ q^2$. Details of these functions can be found in [29,26]. L_c seems to be larger than 500 nm. Therefore, the aggregates are WLMs, and the contour length is set at a larger value $L_c \gg 1/q_{min}$. To reduce the fitting parameters, we use the cross-section radius R_{CS} obtained above and the D_2O scattering length density for contrast ($\rho_{D_2O} = 6.4 \times 10^{10}$ cm^{-2}). The solid line in Fig. 2 corresponds to the flexible cylinder model fitting with a Kuhn length of 77.0 nm, i.e., l_p = 38.8 nm. Our l_p value is similar to previous results obtained for WLMs of conventional surfactants in the semidilute regime [25].

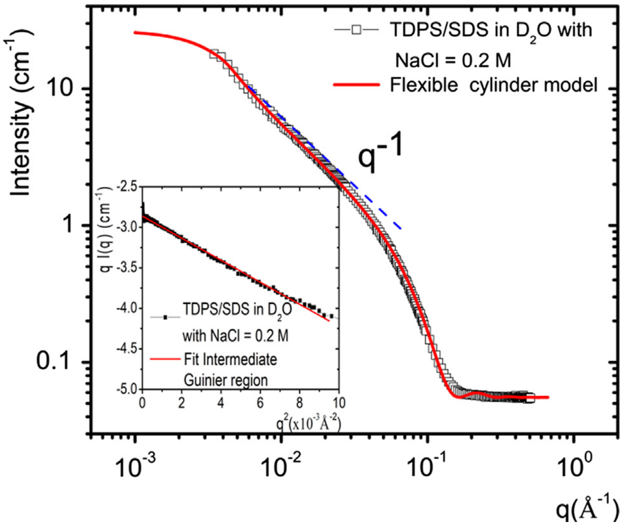

Fig. 2. Static SANS intensity function *vs.* the scattering vector q for TDPS/SDS in a deuterated water solution (C_z = 5 mmol/L, R = 0.55 C_{NaCl} = 0.2 mol/L) at 20 °C. Experimental points (black squares), and fitting for the flexible cylinder model (solid red line). Blue dashed line: q^{-1} slope. Inset: Intermediate Guinier plot and its linear fit to estimate the cross-section radius.

3.1.2. Scanning electron microscopy results

Negatively stained samples of the micellar solution of TDPS/SDS are examined with SEM. Fig. SM6 presents some images of our observations at very large amplifications. Long cylinders are easily observed with a diameter that can be measured on the images. The average diameter of these cylinders is ~3.38 ± 0.08 nm, which is close to the diameter measured with SANS (~4.7 ± 0.01 nm). The observed structure agrees with the results given by SANS. Details in the SM.

3.2. Rheological and Rheo-SANS Results.

3.2.1. Rheology

2.2.2. The rheological properties of the micellar solution are already known; [6,7,25] the main features can be found in Figs. SM1 and SM2. Rheology does not significantly change when the protonated water is exchanged with deuterated water (D_2O), and it does not depend on the instrument that is used or geometry. As an example, Fig. SM3 shows the viscoelastic spectra of the system in H_2O and D_2O. As mentioned in the description of Fig. 1, increasing the shear rate of the isotropic fluid beyond a specific point, the system shear thins, and an aligned phase (paranematic) begins to appear. Hysteresis in thixotropic loops was not significative. In Fig. 1a, the shear-thinning feature is illustrated for TDPS/SDS/D_2O with NaCl at R = 0.55 and C_z = 46 mmol/L at T = 40 °C, although, it is also visible at T = 25 °C (Fig. 1b).

3.2.2. Rheo-SANS

SANS experiments on micellar solutions are performed under shear in a Couette geometry to quantify the structural changes in the system, especially during its shear-thinning. A sketch of the experimental instrument is presented in Fig. 3a. Fig. 3b presents a scheme with SANS patterns obtained at two positions in the gap. Fig. 3c presents some 2D scattering patterns corresponding to specific gap positions (r/H) as a function of the applied $\dot{\gamma}$. Here, r corresponds to the radial distance measured from the inner

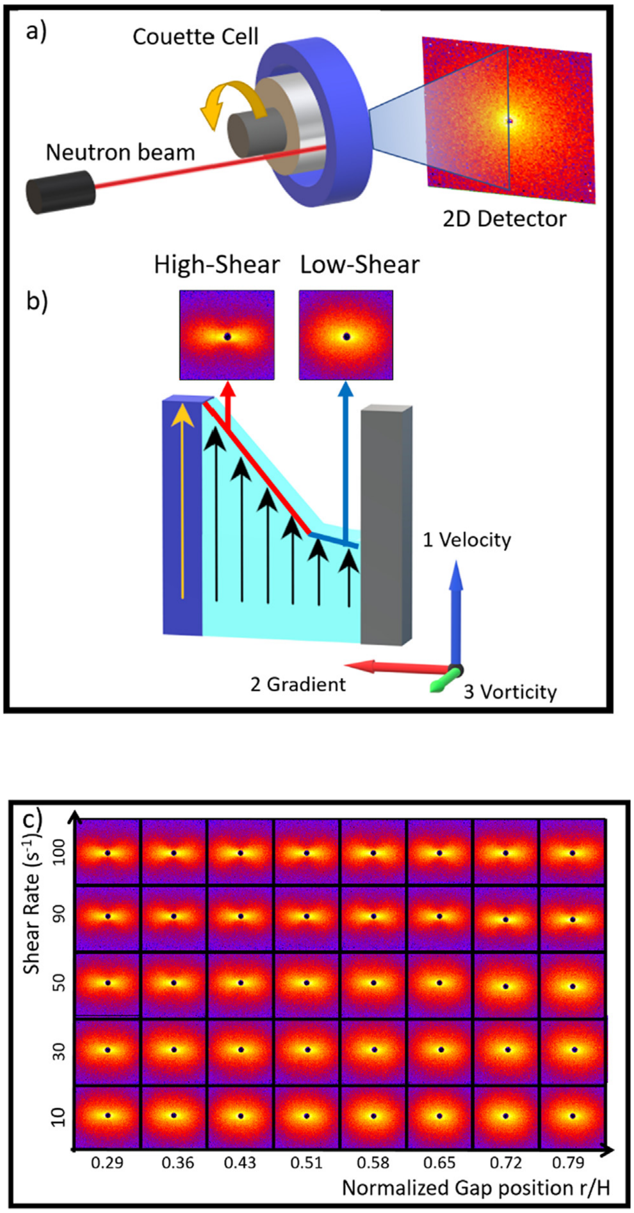

Fig. 3. (a) Sketch of the instrument: A well-characterized neutron beam is sent into the gap of a Couette geometry perpendicular to the 1–2 plane. The cell is filled with a micellar solution at a constant temperature. (b) As the beam passes through a specific position along the gap of a cell filled with a fluid presenting gradient shear bands, it produces a 2D-SANS pattern depending on the structural order in that position. (c) Scattering patterns through the 1–2 plane as a function of the normalized gap position in the shear banding regime ($0.06\ s^{-1} < \dot{\gamma} < 100\ s^{-1}$) for a micellar solution at $T = 40\ °C$ ($C_z = 46$ mmol/L, $R = 0.55$, and $C_{NaCl} = 0.2$ mol/L). r/H = 0 corresponds to the edge moving cylinder.

cylinder, along the gap of total length $H = 1.35$ mm. The beam center moves from close to the inner rotating cylinder, where $r/H \sim 0$, to the inside face of the outer cylinder, $r/H \sim 1$. SANS measurements are made descending the shear rate from 1500 s^{-1} to 10 s^{-1}. At low $\dot{\gamma}$ values and large r/H values, the scattering patterns are isotropic, indicating that the micelles in the network are randomly oriented, as in the sketch of Fig. 3b. As $\dot{\gamma}$increases, far from the moving cylinder wall, the scattering patterns are still isotropic. However, close to the moving cylinder wall, the fluid presents anisotropic scattering patterns that reveal some alignment in this sector of the fluid due to the shear (see rows in Fig. 3c). As $\dot{\gamma}$ increases, the sector of the fluid with aligned WLMs steadily grows up to fulfill the whole gap of the geometry. In Fig. 3c, vertical columns correspond to a specific position in the gap. At any value of r/H, it is easy to observe that at low values of $\dot{\gamma}$, the fluid pattern is less anisotropic than when the shear rate increases.

To quantitatively determine the degree of alignment of the WLMs in the bands, it is useful to calculate an annular intensity function from the 2D corrected scattering patterns (subtracting background). This is a function of the azimuthal angle φ, $I(q^*, \varphi)$. This angle-dependent intensity is performed over a narrow q-range ($0.01 < q < 0.02$ Å^{-1}) centered around $q^* = 0.015$ Å^{-1} that corresponds to the lowest accessible scattering angles probing the most significant possible dimension of the WLMs, *i.e.*, where the static scattering pattern displays a $\sim q^{-1}$ dependence. Some examples of these annular intensity functions are shown in Fig. 4. An orientation distribution function, $F(q^*, \varphi^*)$ that describes the distribution of the tilt angles of the individual tubular micelles, with respect to the shearing velocity axis, is obtained by fitting the annular intensity function to a Legendre series expansion as described by Burger et al. [33] $F(q^*, \varphi^*) = \sum_{n=0}^{\infty} a_n P_{2n}(cos\varphi^*)$, where $\varphi^* = \varphi - (\varphi_o + \pi/2)$. In this formula, only the polynomials with even n need to be considered due to symmetry constraints, $a_0 = 1$ due to the normalization of $F(q^*, \varphi^*)$. φ_o is the mean angle of alignment obtained directly from the annular average that is measured relative to the shear direction. We applied this phase shift to make that the maximum intensity of the annular average occurs at $\varphi^* = 0$. The important fact for us is that the coefficient a_1 is related to Hermans' orientation parameter $\langle P_2\rangle$, also known as the nematic orientation parameter, that is defined as:

$$\langle P_2\rangle = \int_0^\infty \frac{3\cos^2\beta - 1}{2} g(\beta) sen\beta d\beta = \frac{a_1}{5}$$

which take the values of $\langle P_2\rangle = 1$ for perfect parallel orientation, and $\langle P_2\rangle = 0$ for totally random orientation. We use the first five terms of the series to fit the angular distributions. With the resulting fittings, Fig. 5 presents $\langle P_2\rangle$ *vs.* r/H for several shear rate values. Here, depending on the shear rate, $\langle P_2\rangle$ is larger for the WLMs that are close to the moving cylinder, and smaller for those close to the static cylinder. Hence, the fluid under shearing is separated into two sectors. One sector has a high orientational order (aligned or paranematic phase), and another sector with a low orientational order (isotropic phase). These sectors correspond to gradient shear bands that are clearly observed in Fig. 5 at $\dot{\gamma} = 10$, 15, and 20 s^{-1}. As the shear increases, the fluid in the whole gap is aligned. Curiously, the orientation parameter reaches a value of $\langle P_2\rangle \sim 0.40$, which is far from being perfect alignment. This is probably due to the large size of the micelles. L_C has been estimated for these micelles to be ≥ 5 µm, at this NaCl concentration [25].

Counter-intuitively, as the shear rate further increases, it does not imply that $\langle P_2\rangle$ also increases. As shown in Fig. 6, close to the moving cylinder at $r/H = 0.36$, after $\dot{\gamma} \sim 100\ s^{-1}$, $\langle P_2\rangle$ decrease, reaching a minimum value around $\dot{\gamma} \sim 400\ s^{-1}$. $\langle P_2\rangle$ again starts to increase linearly around a $\dot{\gamma}$ value between 400 s^{-1} and 500 s^{-1}. In this figure, we also include different rheological deformation histories for nominally identical samples. The shear histories were made sweeping up and down $\dot{\gamma}$, showing an excellent level of repeatability for $\langle P_2\rangle$ at each value of $\dot{\gamma}$. Therefore, the described behavior is quite robust, and it clearly defines three regions: II, III, and IV. The inset of Fig. 6 also presents a comparison of the orientation parameter with another gap position, $r/H = 0.72$. At other r/H values, the same trend is followed. Histories labeled as *down* and *up* were part of the same sweeping cycle. They were separated just to show the repeatability of the measurements.

After $\dot{\gamma} \sim 100\ s^{-1}$, as $\dot{\gamma}$ increases ($100\ s^{-1} < \dot{\gamma} < 500\ s^{-1}$), a loss of order is observed in the fluid. Viscosity remains constant, or it is slightly thinning. The slope is smaller than those for previous val-

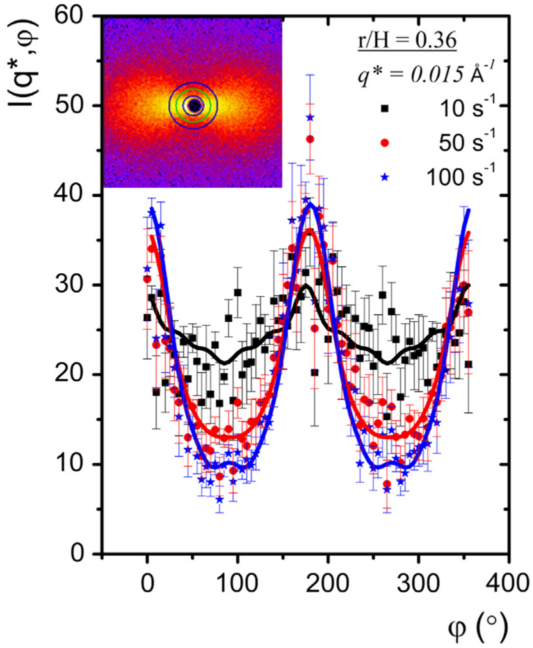

Fig. 4. Examples of annular intensity *vs.* azimuthal angle of 2D Rheo-SANS patterns for a micellar solution in D_2O (C_z = 46 mmol/L, *R = 0.55*, and C_{NaCl} = 0.2 mol/L, *T* = 40 °C) at $\dot{\gamma}$ = 10, 50 and 100 s^{-1}. Lines correspond to the Legendre expansion fits. Inset: An example of an anisotropic SANS pattern.

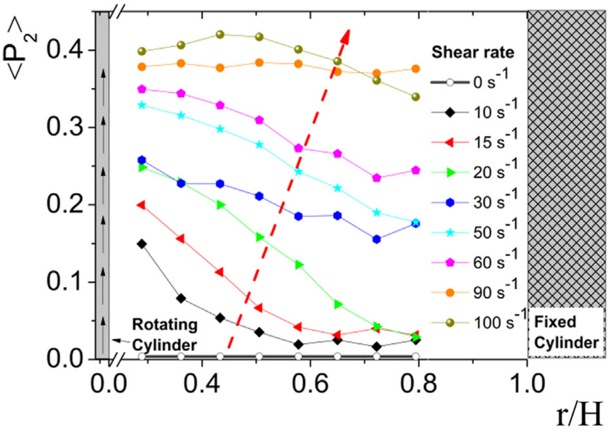

Fig. 5. Orientation parameter of a micellar solution (C_z = 46 mmol/L, *R* = 0.55, and C_{NaCl} = 0.2 mol/L, *T* = 40 °C) at different positions in the gap of the Couette geometry at different shear rates. The red dashed arrow indicates that as shear rate increases, the order in the fluid also rises. Colored lines are guides to the eye.

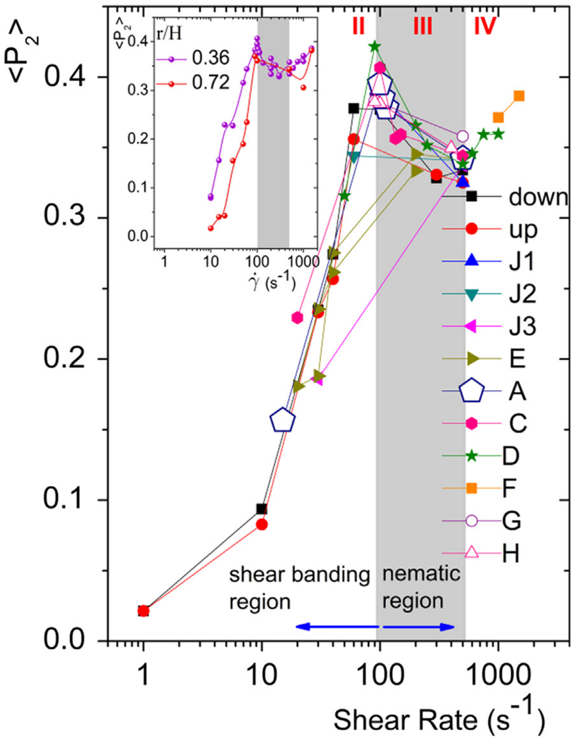

Fig. 6. ⟨P_2⟩ *vs.* $\dot{\gamma}$ for different rheological deformation histories at *r/H = 0.36* and *T* = 40 °C. Shear-flow histories: down: $\dot{\gamma}$ = 500–300–100–60–40–30–10–1 s^{-1}; up: $\dot{\gamma}$ = 1–10–30–40–60–300–500 s^{-1}; J1: $\dot{\gamma}$ = 500–60 s^{-1}; J2: $\dot{\gamma}$ = 500–60 s^{-1}; J3: $\dot{\gamma}$ = 500–30 s^{-1}; E: $\dot{\gamma}$ = 500–200–40–30–20–30–40–200 s^{-1}; A: $\dot{\gamma}$ = 500–113–105–100–15 s^{-1}; C: $\dot{\gamma}$ = 500–150–135–100–20 s^{-1}; D: $\dot{\gamma}$ = 1000–750–600–500–250–200–90 s^{-1}; F: $\dot{\gamma}$ = 1500–1000 s^{-1}; G: $\dot{\gamma}$ = 500–90 s^{-1}; H: $\dot{\gamma}$ = 400–100 s^{-1}. Inset: The orientation parameter at two different gap positions, *r/H* = 0.36 and *r/H* = 0.72.

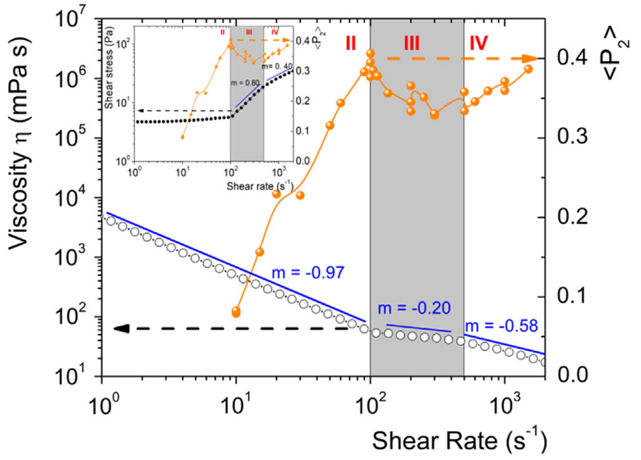

Fig. 7. Viscosity *vs.* $\dot{\gamma}$, and ⟨P_2⟩*vs.*$\dot{\gamma}$ close to the moving cylinder, *r/H* = 0.36, for the micellar solution at *T* = 40 °C. Straight blue lines are guides to the eye to observe the slope change in the viscosity and gold lines are also guides to the eye. Inset: σ and ⟨P_2⟩ *vs.* $\dot{\gamma}$. Viscosity and shear stress were measured with a ME 21 Mooney-Eward Cony cylinder.

ues of $\dot{\gamma}$, see Fig. 7. The shape of the flow curves of σ *vs.* $\dot{\gamma}$ (inset of Fig. 7), also records the change among regions. If $\dot{\gamma}$ increases beyond the minimum value reached by the orientation parameter at 400 s^{-1} <$\dot{\gamma}$ <500 s^{-1}, the viscosity shear thins again but more strongly. The described behavior occurs at *T = 40 °C*, although a similar behavior is found at *25 °C* (see graphs in Figs. SM4 and SM5). Here, the region II starts at 2×10^{-3} s^{-1}, region III at 25 s^{-1}, and region IV at 100 s^{-1}.

Fig. 8 presents the evolution of the orientation parameter in the regime when the shear rate increases at very high values, above $\dot{\gamma} \sim 100$ s^{-1}. Here, the fluid is already fully paranematic (region III). As noted before at $\dot{\gamma} \sim 100$ s^{-1}, the orientation parameter of the aligned fluid reaches a maximum value of ~0.43. However, at higher shear rates in region III, ⟨P_2⟩ decreases and reaches a minimum at $\dot{\gamma} \sim 500$ s^{-1}, where region IV starts. From here, ⟨P_2⟩ starts to increase again. However, it is interesting to note at $\dot{\gamma} \sim 1000$ s^{-1}, we observe inhomogeneous alignment along the gap, as in typical shear banding at lower $\dot{\gamma}$. At $\dot{\gamma} \sim 1500$ s^{-1}, the orientation parameter reaches an almost constant value for all the positions.

It is not easy to explain these unexpected Rheo-SANS results at high shear rates. In the shear-banding region, two nonequilibrium fluids coexist (region II). The isotropic one, with a very small orientation parameter, and another one with a larger orientation

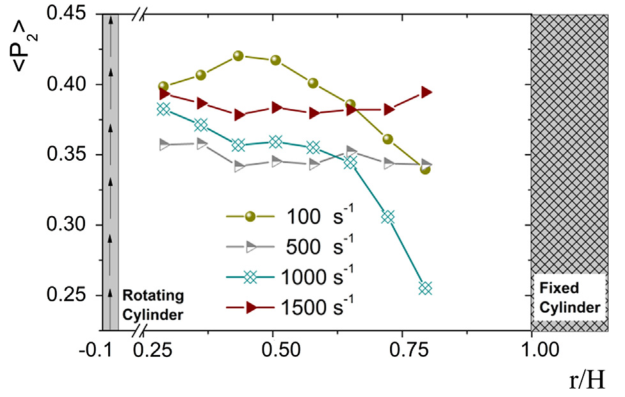

Fig. 8. $\langle P_2\rangle$ *vs.* normalized gap position at high shear rates. 100 s^{-1} $<\dot{\gamma}$ <500 s^{-1} correspond to the limits of region III, and region IV at $\dot{\gamma} > 500$ s^{-1}. Lines are guides to the eye.

parameter, i.e., with aligned structures. As $\dot{\gamma}$ increases, the amount of the aligned phase increases, according to previous studies, approximately following the lever rule [7]. At ~ 100 s^{-1}, there is a change that defines the beginning of region III, where viscosity is almost constant or slightly thinning, and the orientation parameter decreases. At high shear rates, simulation methods for WLMs using a coarse-grained Brownian dynamics model [34] have shown that increasing the shear rate beyond a specific critical shear rate, the contour length decreases and the breaking rate increases. Indeed, this critical shear rate decreases with increasing the scission energy, which in our system is large, [7] because WLMs with higher scission energy have a longer contour length; therefore, they are more easily disturbed by the shear flow. The breaking of WLMs is enhanced due to the additional tension on the micelles, and this effect is also more critical for larger micelles. Therefore, the shear-induced breaking may become important for real WLMs at moderate shear rates. Although the simulations were developed for WLMs made of EHCAC (erucyl bis-(hydroxyethyl) methylammonium chloride), this coarse grained-model is generic, and it can be used in our case to give us a trend of the WLM behavior. Of course, simulations cannot coincide with actual experimental values. In our region II for shear-thinning, simulated shear viscosities *vs.* shear rate predict a universal linear behavior for the log η *vs.* $\dot{\gamma}$ curve, with a slope $m = -1$. According to these simulations in region IV, the relation between log η *vs.* $\dot{\gamma}$ should also be linear and with a slope $m = -2/3$. The experimental values in our experiments at $T = 40$ °C, give -0.97 and -0.58 for regions II and IV, respectively. At $T = 25$ °C, the slope values for regions II and IV are -0.93 and -0.53, respectively. The experimental values for these slopes are very close to those predicted by simulations. Simulations also present a sort of small transition region with a slope similar to what is observed experimentally in region III, but it was not discussed in Ref. [34]. In our region III, the slopes m of log η *vs.* $\dot{\gamma}$ curves are quite small; in our system, they are -0.20 at 40 °C and -0.05 at 25 °C.

At the same time, at high shear rates of the order of 1000 s^{-1} or higher, the mentioned simulations predict a steady-state shear stress which increases with the shear rate as a power law, $\sigma \sim \dot{\gamma}^{\alpha}$, with $\alpha = 1/3$. In our case, inset of Fig. 7, and Fig. SM3, the experimental exponents are 0.40 at 40 °C, and 0.44 at 25 °C; both values are close to the predicted α. The reason for observing this exponent is currently unknown. However, the authors of the mentioned simulations propose that it is related to a balance between the large shear forces tending to break up the WLMs into pieces, smaller than the entanglement length, and the strong alignment that reduces the 'grip' of flow of these micelles. Therefore, considering the information given by simulations, we would expect that WLMs in region III start to break due to friction, *i.e.*, shortening micelles produce a lower constant viscosity or the fluid slightly thins. However, as micellar breaking increases due to the entropic force, micelles make coils that mess up the ordered flow prevalent before the rupture of the WLMs, as in folding-stretching of polymers under elongational flow [35]. As a consequence, the orientation parameter decreases, and the viscosity starts to fall. Increasing the shear rate, as is the case of region IV, the shortened micelles equilibrate to the local conditions of the surrounding media, elongate again and realign correctly. Now, the shear-thinning can be recovered, in a similar way to the case of the shear-thinning of region II. The shear-thinning observed in our system at high shear rates is not unique, one can observe it in other systems, although, it passed unnoticed because it is usually at the limit of the rheological or SANS measurements [7,36,37].

In microfluidic geometries, flow instabilities have been reported in WLM solutions.[38] In viscoelastic fluids, the steady azimuthal Couette flow can be unstable, but instabilities are not governed just by inertia as in simple Newtonian fluids, where $Wi \sim 0$. Wi numbers at which instability transitions occur increase with the elasticity number, Wi/Re, where Re = Reynolds number. Here, there are other routes to flow instabilities because of the single stress relaxation time, τ, dominates the linear viscoelastic regime and brings up an additional time scale. In Couette flow at high shear rates, region IV, the elastic component of the fluid is very large, $Wi = 3440$ while $Re = \rho H^2/\eta \sim 5$; ρ is the fluid density. Then, it would be not strange to observe flow instabilities here. If both Re and Wi are relevant, it appears less known flow instabilities referred to as inertio-elastic. This could open another possibility to explain the loss of order at high shear rates, namely, flow transitions from a pure azimuthal Couette flow to a steady, and then to an unsteady vortex flow. Elastically dominated turbulence has been observed in a homogeneous WLM solution not presenting shear banding, at conditions when inertia is negligible.[39] The transition goes from the purely azimuthal Couette flow to a steady flow; this occurs at low Taylor numbers $Ta = [d/R_i]^{1/2}$ $[\tau\dot{\gamma}] \sim 22–40$.[39] However, as far as we know, inertio-elastic instabilities have been studied just at low Ta numbers.[39,40], not at high Ta, as in our case, where Ta ~ 845. However, H. Mohammadigoushki and S. J. Muller [40] found transitions from a steady flow to a chaotic regime after the shear banding, when the shear rate increased. This quite interesting line of research should be followed soon.

4. Conclusion

TDPS/SDS micelle solutions ($R = [SDS]$ / $[TDPS] = 0.55$) self-assemble in wormlike micelles. This assembling was suspected before, [6,7,25] we now have clear evidence. This system presents a simple shear banding scenario. SANS patterns and orientation parameters of nonequilibrium phases along the shear banding were obtained, showing a clear-cut between isotropic and paranematic phases. At very high shear rates, at the end of the isotropic-paranematic non-equilibrium transition, when the shear rate is steadily increasing, the paranematic fluid viscosity is constant or slightly thinning (100 s^{-1} $<\dot{\gamma}$ <500 s^{-1}), and its orientation order decays. If the shear rate increases even more (500 s^{-1} $<\dot{\gamma}$ <1200 s^{-1}), the fluid shear thins and the orientational order also increases.

Using rheology combined with Small-Angle Neutron Scattering (Rheo-SANS), we could determine the local structural order in the micelle solutions in flow and quiescent. When the shear rate increases at very high shear rates, where the micellar solution is supposed to be aligned, it presents two regions; one where the orientation parameter decays, and a second one where this parameter linearly increases again. In other systems, this region with shear-thinning was observed, [7,36,37,41] but as far as we know, nobody has studied or discussed it. The origin of these regions is not clear, but we presented possible explanations of why we observe them. Increasing the shear rate, at very high values as in region III, the breaking rate increases due to friction, and the contour length decreases; the fluid slightly thins, or viscosity is almost constant. Here, micellar breaking is important, and there is a sudden shortening of the micelles due to the entropic force that instantaneously tries to make it a coil that messes up the ordered flow prevalent before the rupture of the WLMs. As a consequence, in this region III, the orientation parameter decreases. Then, the shortened micelles equilibrate to the local conditions of the surrounding media, elongate again, and realign properly in region IV. We also considered inertio-elastic instabilities as the source of the loss of order.

We consider that this work motivates the study of WLM under shear with simulation methods at very high shear rates. They will help to determine if there are regions where increasing the shear rate produces that the micelle contour length decreases and its breaking rate increases, as well as if the orientational order shows a behavior similar to that mentioned here.

Declaration of Competing Interest

The authors declare that they have no known competing financial interests or personal relationships that could have appeared to influence the work reported in this paper.

Acknowledgements

Financial support from SEP-CONACyT (Projects: Infraest. 280010, FC 076, and 237425), DGAPA-UNAM (IN 106218), and PRODEP (B. A.-G. postdoctoral fellowship) are gratefully acknowledged. We also thank Dr. S. Tehuacanero-Cuapa for his help to get SEM images. Y.L. acknowledges support from the Center for High-Resolution Neutron Scattering (CHRNS), a partnership between NIST and NSF under 479 Agreement No. DMR-1508249.

Disclaimer. Specific commercial equipment, instruments, or materials (or suppliers, or software, ...) are identified in this paper to foster understanding. That identification does not imply recommendation or endorsement by the National Institute of Standards and Technology, nor it does imply that the materials or equipment identified are necessarily the best available for the purpose.

Appendix A. Supplementary material

Supplementary data to this article can be found online at https://doi.org/10.1016/j.jcis.2019.10.052.

References

[1] K. Dhont, W.J. Briels, Rheol. Acta. 47 (2008) 257.
[2] S.M. Fielding, Soft Matter 3 (2007) 1262.
[3] H. Rehage, H. Hoffmann, Molec. Phys. 74 (1991) 933.
[4] R. Makhloufi, J.P. Decruppe, A. Aït-Aliand, R. Cressel, Europhys. Lett. 32 (1995) 253.
[5] J.P. Decruppe, R. Cressely, R. Makhloufi, E. Cappelaere, Polym. Sci. 273 (1995) 346.
[6] D. Lopez-Diaz, E. Sarmiento-Gómez, C. Garza, R. Castillo, J. Col. Interf. Sci. 348 (2010) 152.
[7] D. Lopez-Diaz, R. Castillo, J. Phys. Chem. B 114 (2010) 8917.
[8] P.T. Callaghan, Rheol. Acta 47 (2008) 243.
[9] C. Caiazza, V. Preziosi, G. Tomaiuolo, D. O'Sullivan, V. Guida, S. Guido, J. Coll. Interf. Sci. 534 (2019) 695.
[10] J.J. Cardiel, A.C. Dohnalkova, N. Dubasha, Y. Zhao, P. Cheung, A.Q. Shen, Proc. Natl. Acad. Sci. 110 (E 1653) (2013).
[11] Y. Zh ao, A. Q. Shen, S. J. Haward., Soft Matter 12 (2016) 8666.
[12] S. Lerouge, J.P. Decruppe, C. Humbert, Phys. Rev. Lett. 81 (1998) 5457.
[13] L. Bécu, D. Anache, S. Manneville, A. Colin, Phys. Rev. E 76 (2007) 11503.
[14] M.A. Calabrese, N. Wagner, New Insights from Rheo-Small-Angle Neutron Scattering, in: C.A. Dreiss, Y. Feng (Eds.), Wormlike Micelles, Royal Soc. of Chem., London, 2017.
[15] A.P.R. Eberle, L. Porcar, Cur. Op. Coll. Interf. Sci. 17 (2012) 33.
[16] S. Lerouge, J.F. Berret, Shear-Induced Transitions and Instabilities in Surfactant Wormlike Micelles, in: K. Dusek, J.F. Joanny (Eds.), Polymer Characterization. Adv. in Polym. Sci., Springer, Berlin, 2009.
[17] J.-B. Salmon, A. Colin, S. Manneville, F. Molino, Phys. Rev. Lett. 90 (2003) 228303.
[18] J. Delgado, H. Kriegs, R. Castillo, J. Phys. Chem. B 113 (2009) 15485.
[19] Th. Gallot, C. Perge, V. Grenard, M.A. Fardin, N. Taberlet, S. Manneville, Rev. Sci. Instrum. 84 (2013) 45107.
[20] M.E. Helgeson, M.D. Reichert, Y.Th. Hu, N.J. Wagner, Soft Matter 5 (2009) 3858.
[21] P.D. Olmsted, O. Radulescu, C.-Y.D. Lu, J. Rheol. 44 (2000) 257.
[22] S.M. Fielding, P.D. Olmsted, Eur. Phys. J. E 11 (2003) 65.
[23] S.A. Rogers, M.A. Calabrese, N.J. Wagner, Curr. Opin. Coll. Interf. Sci. 19 (2014) 530.
[24] M.A. Calabrese, S.A. Rogers, L. Porcar, N. Wagner, J. Rheol. 80 (2016) 1001.
[25] E. Sarmiento-Gomez, D. Lopez-Diaz, R. Castillo, J. Phys. Chem. B 114 (2010) 12193.
[26] S.R.J. Kline, Appl. Cryst. 39 (2006) 895.
[27] J.S. Pedersen, P. Schurtenberger, Macromol. 29 (1996) 7602.
[28] M.W. Liberatone, F. Nettesheim, N.J. Wagner, L. Porcar, Phys. Rev. E 73 (2006) 20504.
[29] Y. Zhao, A.M. Jamieson, B.G. Olson, N. Yao, S. Dong, S. Nazarenko, X. Hu, J. Lal, J. Polym. Sci. B. 44 (2006) 2412.
[30] C.A. Dreiss, Soft Matter 3 (2007) 956.
[31] B. Hammouda, J. Appl. Cryst. 43 (2010) 716.
[32] W.-R. Chen, P.D. Butler, L.J. Magid, Langmuir 22 (2006) 6539.
[33] C. Burger, B.S. Hsiao, B. Chu, J. Macromolec. Sci. 50 (2010) 91.
[34] J.T. Padding, E.S. Boek, W.J. Briels, J. Chem. Phys. 129 (2008) 074903.
[35] A. Alexander-Katz, M.F. Schneider, S.W. Schneider, A. Wixforth, R.R. Netz, Phys. Rev. Lett. 97 (2006) 138101.
[36] J.J. Cardiel, D. Takagi, H.-F. Tsai, A.Q. Shen, Soft Matter 12 (2016) 8226.
[37] M.R. Rojas, S.A. Müller, A.E. Sáez, J. Coll. Interf. Sci. 326 (2008) 221.
[38] N. Dubash, P. Cheung, A.Q. Shen, Soft Matter 8 (2012) 5847.
[39] C. Perge, M.A. Fardin, S. Manneville, Soft Matter 10 (2014) 1450.
[40] H. Mohammadigoushki, S.J. Muller, J. Rheol. 61 (2017) 683.
[41] J.T. Padding, W.J. Briels, M.R. Stukan, E.S. Boek, Soft Matter 5 (2009) 4367.